magnetochemistry

MDPI

Article

New Silver(I) Coordination Polymer with Fe_4 Single-Molecule Magnets as Long Spacer

Luca Rigamonti [1,*], Manuela Vaccari [1], Fabrizio Roncaglia [1], Carlo Baschieri [1] and Alessandra Forni [2]

[1] Dipartimento di Scienze Chimiche e Geologiche, Università degli Studi di Modena e Reggio Emilia, via G. Campi 103, 41125 Modena, Italy; manu_sam@hotmail.it (M.V.); fabrizio.roncaglia@unimore.it (F.R.); carlo.baschieri@unimore.it (C.B.)

[2] Istituto di Scienze e Tecnologie Molecolari, Consiglio Nazionale delle Ricerche (ISTM-CNR), via C. Golgi 19, 20133 Milano, Italy; a.forni@istm.cnr.it

* Correspondence: luca.rigamonti@unimore.it or luca.rigamonti@yahoo.com

Received: 11 May 2018; Accepted: 25 September 2018; Published: 1 October 2018

Abstract: In continuation of our work on supramolecular architectures of single-molecule magnets (SMMs) as a promising strategy in developing their magnetic performance, in this paper we report the synthesis and single crystal X-ray structure of the centered triangular tetrairon(III) SMM, $[Fe_4(PhPy)_2(dpm)_6]$, **Fe_4** (Hdpm = dipivaloylmethane, **H_3PhPy** = 2-(hydroxymethyl)-2-(4-(pyridine-4-yl)phenyl)propane-1,3-diol), and its assembly in the coordination polymer $\{[Fe_4(PhPy)_2(dpm)_6Ag](ClO_4)\}_n$, **$Fe_4$Ag**, upon reaction with silver(I) perchlorate. Thanks to the presence of the pyridyl rings on the two tripodal ligands, **Fe_4** behaves as divergent ditopic linker, and due to the **Fe_4**:$AgClO_4$ 1:1 ratio, **Fe_4Ag** probably possesses a linear arrangement in which silver(I) ions are linearly coordinated by two nitrogen atoms, forming 1D chains whose positive charge is balanced by the perchlorate anions. The stabilization of such a polymeric structure can be ascribed to the long distance between the two donor nitrogen atoms (23.4 Å) and their donor power. **Fe_4Ag** shows slow relaxation of the magnetization which follows a thermally activated process with U_{eff}/k_B = 11.17(18) K, τ_0 = 2.24(17) 10^{-7} s in zero field, and U_{eff}/k_B = 14.49(5) K, τ_0 = 3.88(8) 10^{-7} s in 1-kOe applied field, in line with what reported for tetrairon(III) SMMs acting as building blocks in polymeric structures.

Keywords: single-molecule magnets; iron; silver; magnetic properties; coordination polymer

1. Introduction

Single-molecule magnets (SMMs) [1], thanks to their directionally bistable magnetic moment, have been investigated over the last two decades as nanoscale, chemically tunable entities for encoding binary information. Though SMMs developed so far show slow relaxation of the magnetization only at low temperatures (below liquid nitrogen), preventing their application in spintronics devices [2], a fast increase of their performance is expected, as recently shown through the synthesis of a dysprosocenium complex with opening of magnetic hysteresis at a temperature as high as 60 K [3,4]. Another promising strategy to develop SMM features consists of the assembly into extended coordination networks [5–10], which may allow enhanced magnetic remanence due to intramolecular magnetic coupling [11].

Complexes of the family of tetrairon(III) SMMs with general formula $[Fe_4(L)_2(dpm)_6]$ [12–14] (H_3L = tripodal ligand, Hdpm = dipivaloylmethane) include four coplanar high spin iron(III) ions (s = 5/2) forming a centered triangular geometry. The central metal atom (Fe^c) is antiferromagnetically coupled to the three peripheral ones (Fe^p) so as to give an S = 5 spin ground state. In general, clusters of this family feature easy axis anisotropy normal to the metal plane. Despite the low energy

barrier of Fe_4 SMMs reaching up to 15–17 K, their chemical versatility has been exploited by creating clusters able to sublimate by fluorination of the peripheral β-diketonato ligands [15–17] or anchor on gold surfaces by sulfur-rich tripodal ligands [18,19], as well as modulating the spin ground state by selective replacement of the central metal ion with chromium(III) [20,21], vanadium(III) [22], or lanthanide ions [23,24]. This family of SMMs has been also characterized as single-molecule junction in scanning tunneling microscope (STM) experiments at 0.5 K [25] and through theoretical calculations for its behavior in spin-polarized transport [26], revealing how Fe_4 SMMs would be excellent candidates for molecular spintronics devices. Recently, the derivative $[Fe_4(pPy)_2(dpm)_6]$ (**A**) (H_3pPy = 2-(hydroxymethyl)-2-(pyridine-4-yl)propane-1,3-diol) [11] has also revealed to behave as efficient ditopic supramolecular synthon due to the presence of two divergent 4-pyridyl substituents on the tripodal ligands, as formerly found in the assembly of 1D chains by using ruthenium paddlewheel dimers as coordination nodes [11]. By modulating the redox state of the Ru_2 units (II,II vs. II,III), we could introduce a significant exchange bias with intra-chain coupling, and concomitant enhancement of the remnant magnetization. The ability of **A** as building block of supramolecular structures has been further confirmed by reaction with silver(I) perchlorate yielding $\{[Fe_4(pPy)_2(dpm)_6]_2Ag\}(ClO_4)$ (**B**), a tridimensional metal–organic framework (3D-MOF) [14]. In this compound, Ag^+ ions behave as tetrahedral nodes coordinated by four pyridyl nitrogen atoms of Fe_4 units, and the cubic crystals, although with no overall second-order anisotropy, can be persistently magnetized parallel or antiparallel to the four main diagonals of the unit cell.

Compound **B** also possesses accessible voids (14.3% of unit cell volume) able to trap small solvent molecules, which can be exploited as a means for modulating the magnetic properties. However, due to the presence of two interlocked **dia** networks (according to IUPAC nomenclature [27]), the space left inside the 3D-MOF is not available for bigger molecules [14]. In the attempt to build-up a new polymeric structure with larger cavities by elongating the SMM spacer, in this work we synthesized the new tripodal ligand **H_3PhpPy**, 2-(hydroxymethyl)-2-(4-(pyridine-4-yl)phenyl) propane-1,3-diol (Scheme 1), where we added a phenyl ring between the triol unit and the pyridyl terminal fragment with respect to H_3pPy. This ensures the same divergent ditopic linker behavior once incorporated into an Fe_4 SMM, constituting at the same time a longer spacer upon coordination of the pyridyl rings to silver(I) ions. Here we report the synthesis of **H_3PhpPy**, its assembly into $[Fe_4(PhpPy)_2(dpm)_6]$ (**Fe_4**), whose structure was confirmed by single crystal X-ray diffraction studies, and further reaction of **Fe_4** with $AgClO_4$. The behavior as SMM of the resulting coordination polymer $\{[Fe_4(PhpPy)_2(dpm)_6Ag](ClO_4)\}_n$ (**Fe_4Ag**) will be then described, in comparison with the 3D-MOF **B** and the **Fe_4** building block.

2. Results and Discussion

2.1. Synthesis of the Tripodal Ligand H_3PhpPy

Two possible synthetic paths for **H_3PhpPy** were identified, both starting from commercial 2-(4-bromophenyl)ethanol and involving three synthetic steps. The most convenient method proved to be the one featuring a first Suzuki cross-coupling with pyridin-4-ylboronic acid, followed by oxidation of the homobenzylic alcohol and completed by a Tollens addition with paraformaldehyde (Scheme 1). Another variant was also investigated, featuring the oxidation, Tollens and Suzuki sequence, but its efficacy was lower (Scheme S1 in Supplementary Materials).

Following Scheme 1, the cross-coupling reaction between 2-(4-bromophenyl)ethanol and pyridin-4-ylboronic acid was performed on the basis of a procedure reported in the literature [28] by means of $Pd(PPh_3)_4$ as catalyst. The presence of the pyridyl group gave us the opportunity to separate the product **1** from *N*,*N*-dimethylformamide (DMF) by precipitating it as hydrochloride salt, avoiding the use of column chromatography and still guaranteeing good yield and optimal purity as detectable with GC-MS and ^{1}H NMR analyses. The oxidation of **1** was secured with a radical method, employing trichloroisocyanuric acid (TICA) and (2,2,6,6-tetramethylpiperidin-1-yl)oxyl (TEMPO) radical [29],

while other tested methods caused the partial conversion to the more stable benzaldehyde derivative. The following reaction of **2** with paraformaldehyde and $Ca(OH)_2$ in tetrahydrofuran (THF) [29–31] allowed the double aldolic addition and the Cannizzaro reaction to the final tripodal ligand **H_3PhpPy** with a reasonable yield of 41%. The addition of $Al(OiPr)_3$ as additive had not a clear scope in this reaction, but we could observe easier purification of the crude product. The overall yield of the tripodal ligand starting from commercial 2-(4-bromophenyl)ethanol is then 23%.

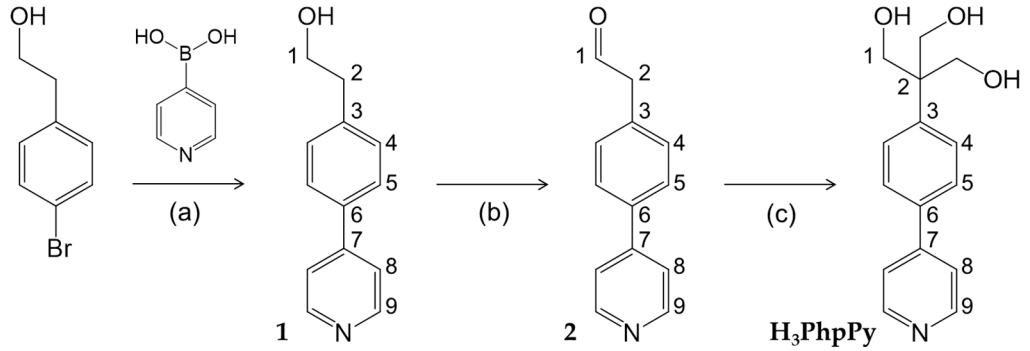

Scheme 1. (**a**) Na_2CO_3, $Pd(PPh_3)_4$, DMF:H_2O 3:1, 110 °C, 24 h (yield: 58%); (**b**) TICA, TEMPO, CH_2Cl_2, 0 °C, 15 min (yield: 95%); (**c**) paraformaldehyde, $Ca(OH)_2$, $Al(OiPr)_3$, THF, 60 °C, 3 days (yield: 41%); overall yield: 23%; atom numbering as used for NMR assignment (see Section 3).

The alternative pathway reported in Scheme S1 in Supplementary Materials was also attempted in order to move the triol-formation step, characterized by the lowest yield, before the cross-coupling. In this way it would have been possible to save on the amount of used palladium catalyst, which is the most expensive reagent in this synthesis. The first oxidation step of 2-(4-bromophenyl)ethanol with TICA and TEMPO led to **3** in very high yield, and the following reaction with paraformaldehyde allowed the isolation of **4** with the formed triol fragment. Unfortunately, the cross-coupling of **4** with pyridin-4-ylboronic acid in the presence of $Pd(PPh_3)_4$ did not yield the desired final tripodal ligand even after several attempts. This might possibly due to an interference of the triol unit that can coordinate the palladium ion, sequestering it from the catalytic cycle, or an interaction between the triol unit and the boronic acid.

2.2. Assembly of **Fe_4** *and Its Molecular Structure*

The assembly of the Fe_4 cluster with **H_3PhpPy** was performed as previously established [11,12] by reacting a solution of $[Fe_4(OMe)_6(dpm)_6]$ [32] in diethyl ether (Et_2O) with the tripodal ligand suspended in ethanol (EtOH). Upon addition of **H_3PhpPy** a darkening of the orange solution could be observed, hint of the exchange of the six bridging methoxido ligands with two tripodal ones. Nevertheless, by vapor diffusion of EtOH with the reaction mixture we could almost always obtain crystals of the dimeric cluster $[Fe_2(OEt)_2(dpm)_4]$ (thermodynamic product), whose formation is known to be favored in basic conditions [33]. Differently from H_3pPy, the inductive effect of the added phenyl ring might pushes electron density toward the pyridyl moiety [34] in the tripodal ligand **H_3PhpPy**, with resulting pronounced basicity.

Nevertheless, we could isolate single crystals of **Fe_4** suitable for X-ray diffraction from the concentrated mother liquor of one synthetic attempt. They belong to the monoclinic space group C_2/c as most of the reported homologous tetrairon(III) clusters [12,13,29], and in particular its shorter analogue **A**·2EtOH [11]. Selected geometrical parameters at 293(2) K are reported in Table 1, and a view of the molecular structure is shown in Figure 1.

The four iron(III) ions define a metal-centered triangle that develops around the crystallographic two-fold axis passing through Fe1 and Fe2. The molecular structure is held together by two tri-deprotonated tripodal ligands that bridge the central ion (Fe1) to the peripheral ones (Fe2, Fe3, Fe3′; primed atom is generated by the two-fold rotation). The coordination sphere of each peripheral

metal ion is completed by two bidentate dpm^- ligands to form the classical propeller-like structure with helical pitch, calculated as dihedral angle between Fe_4 and FeO_2Fe planes, of about 67–69°. Thus, all metal centers achieve a distorted octahedral environment formed by six oxygen atoms with Fe–O distances falling in the 1.97–2.03 Å narrow range. The isosceles triangle given by the peripheral iron(III) ions possesses two long sides (5.3903(11) Å) and a short one (5.2063(15) Å), and no ethanol molecules are involved in hydrogen bonds with the nitrogen atom of the pyridyl ring in the solid state, differently from **A**·2EtOH [11]. Phenyl and pyridyl rings of the tripodal ligand are not co-planar, being rotated each other of 6.47(5)°. The last ones are involved in weak $\pi\cdots\pi$ stacking interactions (the shortest C–C distance is 3.67 Å) that, together with weak hydrogen bonds, contribute to stabilize the overall crystal structure (Figure S1 in Supplementary Materials).

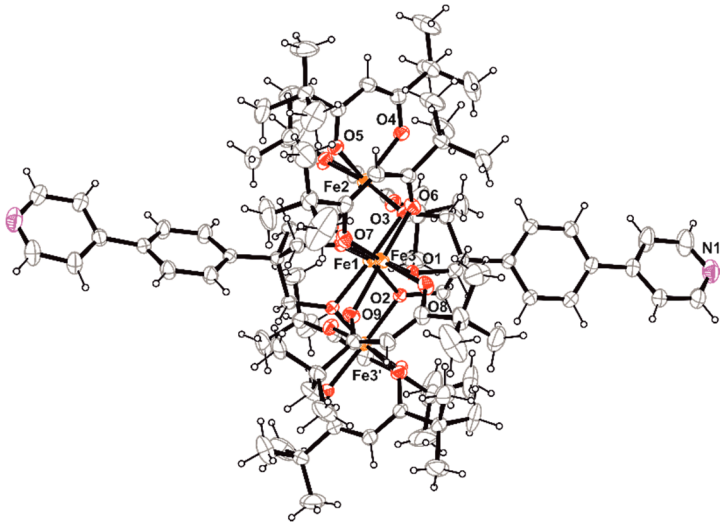

Figure 1. Molecular structure of **Fe_4** with ellipsoids at 20% probability, viewed along the crystallographic *c* axis with atom labelling scheme used in Table 1. Color code: Fe = orange, O = red, N = violet, C = grey, H = black.

Table 1. Selected interatomic distances (Å) and angles (°) in **Fe_4** [1] (see Figure 1 for atom labelling).

Parameter	Value	Parameter	Value	Parameter	Value
Fe1–O1	1.994(3)	Fe2–O4	1.988(3)	Fe1···Fe2	3.0926(12)
Fe1–O2	1.971(2)	Fe2–O5	2.029(3)	Fe1···Fe3	3.0700(8)
Fe1–O3	1.978(2)	Fe3–O6	1.994(3)	Fe2···Fe3	5.3903(11)
Fe2–O3	1.977(2)	Fe3–O7	1.997(3)	Fe3···Fe3′	5.2063(15)
Fe3–O1	1.972(2)	Fe3–O8	1.998(3)	Fe2···Fe1···Fe3	122.014(17)
Fe3–O2	1.989(3)	Fe3–O9	2.005(3)	Fe3···Fe1···Fe3′	115.970(18)
Fe1–O1–Fe3	101.46(11)	Fe1–O2–Fe3	101.66(11)	Fe1–O3–Fe2	102.87(12)
γ (Fe2) [2]	67.16(10)	γ (Fe3) [3]	69.08(8)	N1···N1′	23.413(11)

[1] Primed atoms are related to unprimed ones by the two-fold axis passing through Fe1 and Fe2; [2] Dihedral angle between Fe1,Fe2,Fe3 and Fe1,O3,Fe2 planes; [3] Dihedral angle between Fe1,Fe2,Fe3 and Fe1,O1,O2,Fe3 planes.

Due to the difficulty to isolate the desired cluster as pure crystalline phase, we decided to investigate whether or not **Fe_4** was already formed in solution after 5 h of stirring between $[Fe_4(OMe)_6(dpm)_6]$ and **H_3PypPy**. The reaction mixture was analyzed via ESI-MS spectrometry and we could positively identify the main peaks at m/z = 1874.7 and 1836.8, belonging to the +K and +H positive ions of **Fe_4** (Figure S2 in Supplementary Materials). The only other detected peak appears at m/z = 644.4, which corresponds to $[Fe(dpm)_3 + K]^+$, a decomposition product of $[Fe_4(OMe)_6(dpm)_6]$ upon standing in solution [12]. Proved that the desired cluster is formed in solution (kinetic product), the reaction mixture was then taken to dryness under reduced pressure without heating and the infrared spectrum of the obtained orange solid was compared with the ones

of the dimeric species $[Fe_2(OEt)_2(dpm)_4]$ and the starting cluster $[Fe_4(OMe)_6(dpm)_6]$ (Figure S3 in Supplementary Materials). Even if very similar, the three spectra contain substantial differences in the position and relative intensities of several bands, which all hint to confirm the formation of **Fe$_4$**. In particular, the coordination of the tripodal ligand is supported by the alkoxido C–O stretching band shifted to 1096 from 1050 cm^{-1} in the progenitor tetranuclear cluster $[Fe_4(OMe)_6(dpm)_6]$.

Furthermore, the orange solid was analyzed via ^{1}H NMR spectroscopy dissolving the product in toluene-d_8: the spectrum (Figure S4 in Supplementary Materials) clearly entails the intense broad signal at 10.9 ppm characteristic of the paramagnetically shifted *t*Bu substituents in this kind of Fe_4 complexes [12,15,16]. Other four broad signals at 12.0 (shoulder) 8.8, 8.5 and 6.5 ppm can be observed, ascribable to the corresponding four different aromatic protons of the tripodal ligand; in particular the shoulder at 12.0 ppm can be attributed to H5 (Scheme 1 for atom numbering), in analogy to the known Fe_4 complexes with phenyl substituent [12,16], while the narrower peak at 8.8 ppm should be generated by H9, close to the nitrogen atom of the pyridyl ring and farther from the paramagnetic core. An additional shoulder at 13.1 ppm due to decomposition to $[Fe(dpm)_3]$ is present [12], in agreement with what observed in the ESI spectrum; anyway, this signal is weaker than the ones of the desired main product **Fe$_4$**. Most important, the ^{1}H NMR spectrum remained almost unchanged after 16 h, which allow us to conclude that the desired cluster is stable in toluene and suitable for its subsequent use.

2.3. *Assembly of* **Fe$_4$Ag**

The reaction of **Fe$_4$** with $AgClO_4$ was performed by liquid/liquid diffusion of a toluene solution containing the tetrairon(III) cluster into a THF solution of $AgClO_4$. Regardless of the relative concentration, we could always isolate needle-like microcrystals of **Fe$_4$Ag** with a 1:1 ratio between the two components. This was confirmed by comparing the experimental percentages with the calculated elemental analysis of different stoichiometric combinations, always fitting with the [**Fe$_4$**$AgClO_4$] minimal formula. When using a **Fe$_4$**:$AgClO_4$ 2:1 ratio, the formation of microcrystalline **Fe$_4$Ag** resulted in a darker orange solution containing the excess of unreacted **Fe$_4$**.

The infrared spectrum of **Fe$_4$Ag** fully resembles the one of **Fe$_4$** (Figure S5 in Supplementary Materials), which proves the intactness of the starting tetrairon(III) cluster. The presence of $AgClO_4$ is confirmed by the appearance of a unique perchlorate stretching band at 1122 cm^{-1}, distinctive of an anion in tetrahedral symmetry and purely ionic character [35], as previously observed for **B** [14]. It is also possible to detect a weak band at 479 cm^{-1} tentatively ascribable to the Ag–N bond stretching [36], confirming the coordination of silver(I) by the nitrogen atoms of the pyridyl rings. Another proof can be found in the ESI-MS spectrum of **Fe$_4$Ag** in THF/CH_3CN with the peak at m/z = 2014.7 for the [**Fe$_4$**$Ag(THF)]^+$ ion, in addition to the peaks at m/z = 1836.4 and 1874.8, as previously observed for **Fe$_4$** (Figure S6 in Supplementary Materials). Further confirmation is given by the X-ray fluorescence (XRF) spectrum, where Fe, Ag, and Cl are clearly detected (Figure S7 in Supplementary Materials).

The orange microcrystals of **Fe$_4$Ag** are practically insoluble in all common solvents, clearly suggesting the polymeric nature of the product. It revealed to be soluble only in pyridine, which coordinates silver(I) ions replacing **Fe$_4$**. The **Fe$_4$**:$AgClO_4$ 1:1 ratio, the needle-like crystal habit which resemble the 1D chains with ruthenium paddlewheel dimers [11], the insolubility of the product and the ionic T_d symmetry of the perchlorate anions as given by the infrared spectrum led to identify **Fe$_4$Ag** as a probable linear coordination polymer of silver(I) ions linked together by intact **Fe$_4$** units acting as long spacer (N1···N1′ = 23.413(11) Å), whose positive charge is balanced by ClO_4^- ions occupying voids in between adjacent 1D chains (Scheme 2). The propensity of silver(I) to give linear coordination environment with pyridine [37–39] or nitrogen ligands [40–43] is reported, and in this case the high basicity of the pyridyl ring given by the releasing electronic effect of the attached phenyl ring [34] might convey enough donor power to only two nitrogen atoms in order to satisfy the coordinative electronic demand of silver(I).

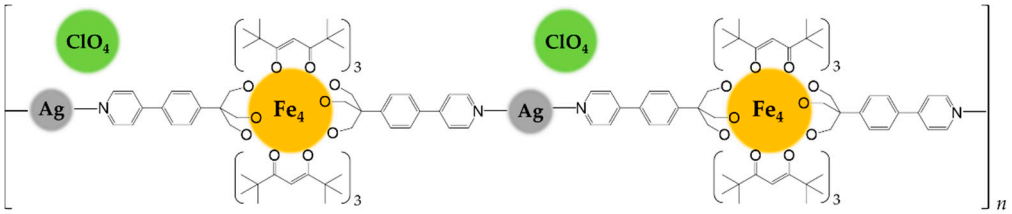

Scheme 2. Representation of **Fe$_4$Ag** as 1D coordination polymer.

2.4. Magnetic Characterization

Thanks to the intactness of Fe_4 units within the polymer and the purity of the crystalline phase as given by elemental analysis and optical microscope inspection, we performed direct current (dc) magnetic measurements on **Fe$_4$Ag**. The temperature dependence of the molar magnetic susceptibility, χ_M, in low fields (1–10 kOe) was measured between 1.9 and 300 K, and the data are reported in Figure 2 as $\chi_M T$ vs. T plot. The shape is characteristic for triangular-centered Fe_4 clusters, where the dominant antiferromagnetic interactions between Fe^c and Fe^p centers lead to an $S = 5$ ground state [12,14,15,32]. The $\chi_M T$ value at room temperature is about 13.0 emu K mol^{-1}, hence lower than the Curie constant for four $s = 5/2$ spins (17.51 emu K mol^{-1} with $g = 2.00$); upon cooling, it first decreases towards a minimum at 95 K (ca. 10.2 emu K mol^{-1}) and then increases again reaching 12.9 emu K mol^{-1} at 8 K, before a further drop at the lowest temperatures. The $\chi_M T$ value at low T is then rising toward the Curie constant for the expected $S = 5$ ground state (15.00 emu K mol^{-1} with $g = 2.00$). Magnetic exchange interactions among the four iron(III) centers are usually obtained by fitting the $\chi_M T$ vs. T curve to a Heisenberg *plus* Zeeman spin Hamiltonian that assumes threefold molecular symmetry to avoid over-parametrization [15]:

$$\hat{H} = J\,(\hat{\mathbf{S}}_1\cdot\hat{\mathbf{S}}_2 + \hat{\mathbf{S}}_1\cdot\hat{\mathbf{S}}_3 + \hat{\mathbf{S}}_1\cdot\hat{\mathbf{S}}_4) + J'\,(\hat{\mathbf{S}}_2\cdot\hat{\mathbf{S}}_3 + \hat{\mathbf{S}}_2\hat{\mathbf{S}}_4 + \hat{\mathbf{S}}_3\hat{\mathbf{S}}_4) + g\mu_B\hat{\mathbf{S}}\cdot\hat{\mathbf{H}} \quad (1)$$

where $\mathbf{S}_1$ is the spin vector for Fe^c; $\mathbf{S}_2$, $\mathbf{S}_3$, and $\mathbf{S}_4$ are the spin vectors for Fe^p ions; $\mathbf{S}$ is the total spin vector; $\mathbf{H}$ is the applied magnetic field; and J and J' coupling constants are the nearest-neighbor (n.n.) and next-nearest-neighbor (n.n.n.) interactions, respectively. Due to the lower increase of the $\chi_M T$ value at low T with respect to the expected Curie constant for the $S = 5$ ground state reported above and the fact that n.n. interactions are most effective in the high-temperature regime, the best-fit procedure was conducted in the 40–300 K range with data obtained with a 10-kOe applied field (filled circles in Figure 2) using PHI program [44], yielding a satisfactorily reproduction of the experimental data with $g = 1.9840(12)$, $J = 13.98(8)$ cm^{-1} and $J' = 0.86(2)$ cm^{-1} (black curve in Figure 2).

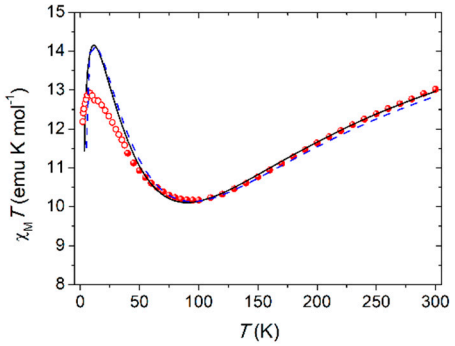

Figure 2. Temperature dependence of $\chi_M T$ for **Fe$_4$Ag**; solid and dashed curves are calculated using the best-fit parameters reported in the text.

These parameters are in line with what reported for the Fe_4 SMM family with isotropic g close to 2.00, as expected for high spin iron(III) ions, and the presence of dominant n.n. antiferromagnetic coupling and J' of one order of magnitude smaller than J [11,12,14,15]. This last coupling constant

is slightly lower than expected (15–19 cm^{-1} [11,13]), but this can be easily envisaged by the lower value of the minimum of the $\chi_M T$ curve, which usually falls between 110 and 120 K in other Fe_4 derivatives [12–14]. Furthermore, the shift to about 90 K of the reproduced minimum from the experimental value of 95 K suggests that the real J might be slightly higher. Correction of this shift was carried out by simulating different curves with J ranging from 12 to 16 cm^{-1}, leaving g and J' unaltered. The best prevision of the minimum in the $\chi_M T$ curve is obtained with J = 14.6 cm^{-1} (dashed blue curve in Figure 2), still maintaining a satisfactory reproduction of the experimental data at $T > 40$ K. Upon further cooling below 40 K, the $\chi_M T$ product (empty circles in Figure 2 obtained with a 1-kOe applied field) follows the expected growing trend toward the Curie constant of the S = 5 ground state, but it is lower than the expected values from the fitting curve, and this can be probably ascribed to the presence of anisotropic effects or weak intermolecular interactions, which are more effective at low temperature.

Even if not isolated as crystalline phase, dc magnetic data were also collected for a powder sample of **Fe_4**, whose elemental analysis closely reproduced the one of the pure compound, in order to perform a direct comparison with **Fe_4Ag**. The temperature dependence of χ_M in low fields (1–10 kOe) was measured between 5 and 250 K, and the data are reported in Figure S8 in Supplementary Materials as $\chi_M T$ vs. T plot. As before, data were well-fitted by means of Equation (1) in the whole temperature range obtaining g = 1.9832(9), J = 15.10(6) cm^{-1}, J' = 0.80(2) cm^{-1}. Differently from **Fe_4Ag**, in the case of **Fe_4** the anisotropic effects at low temperature seem to be negligible; nevertheless, both n.n. and n.n.n. interactions in the polymeric 1D chain are fully comparable with the ones in the progenitor cluster.

The magnetization dynamics of both **Fe_4Ag** and **Fe_4** was then probed with alternating current (ac) susceptibility measurements in zero static field as a function of both temperature (down to 1.9 K) and frequency of the oscillating field (ν = 10–10,000 Hz). Characteristic frequency-dependent maxima in χ''_M vs. T plots were detected, which indicate that **Fe_4Ag** and **Fe_4** behave as SMMs (Figure 3a and Figure S9a in Supplementary Materials). Measurements were then repeated at 1.9 K by applying a static field H in the 0–50 kOe range for **Fe_4Ag** in order to evaluate the most effective field in slowing down relaxation by cutting quantum tunneling (QT) pathways (Figure 3b), and the static field H = 1 kOe was found to be the best option to repeat ac measurements at variable T (Figure 3c for **Fe_4Ag** and Figure S9b in Supplementary Materials for **Fe_4**). Quantitative data treatment was based on a generalized Debye model [45,46] to extract the temperature-dependent relaxation time τ and the width of its distribution α. The model was found to be fully satisfactory and afforded α values that approach 0.20 and 0.23 at H = 0 and 1 kOe, respectively, at the lowest T, while they decrease toward zero at high T for both compounds.

By plotting ln(τ) vs. $1/T$, linear trends can be clearly recognized at both static fields (Figure 3d for **Fe_4Ag** and Figure S9c,d in Supplementary Materials for **Fe_4**), which indicate that reversal of the magnetization proceeds via a thermally activated process in the temperature range analyzed. Data can be suitably fitted by the Arrhenius law $\tau = \tau_0 \exp(U_{eff}/k_B T)$ obtaining U_{eff}/k_B = 11.17(18) K and τ_0 = 2.24(17) 10^{-7} s in zero field, and U_{eff}/k_B = 14.49(5) K and τ_0 = 3.88(8) 10^{-7} s in 1-kOe applied field for **Fe_4Ag**, and U_{eff}/k_B = 10.69(16) K and τ_0 = 7.0(7) 10^{-7} s in zero static field, and U_{eff}/k_B = 14.9(2) K and τ_0 = 5.1(3) 10^{-7} s at 1 kOe for **Fe_4**.

These thermally activated relaxation parameters fully resemble the ones found for the 3D-MOF **B** (τ_0 = 1.65(8) 10^{-7} s and U_{eff}/k_B = 11.46(10) K in zero static field, and τ_0 = 3.21(11) 10^{-7} s and U_{eff}/k_B = 14.25(8) K at 1 kOe) [14], which are similar but lower compared to Fe_4 clusters not involved in coordination networks [12], and especially with **A**·2EtOH [11] as building block of **B** [14]. This seems to confirm the different spin-phonon interactions, which affect the magnetic relaxation [47], between an organized 1D/3D framework and a molecular crystal held together only by van der Waals forces. The values for **Fe_4**, similar to the ones of **Fe_4Ag** and **B** and lower to the ones of **A**·2EtOH [11] and the tetrairon SMM with phenyl rings on the tripodal ligands [12], seems also to suggest that the weak but extended $\pi\cdots\pi$ stacking interactions between the phenylpyridine fragments of adjacent molecules in the crystal packing of **Fe_4** are sufficient to mimic the spin-phonon effect in a coordination polymer.

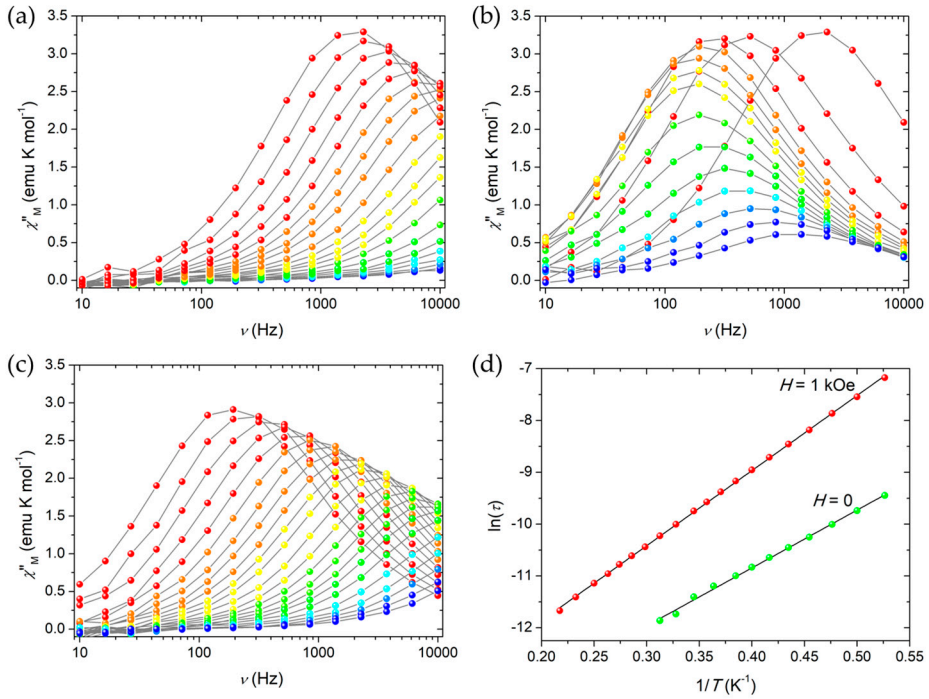

Figure 3. Imaginary component of the ac susceptibility, χ''_M, of **Fe_4Ag** measured at (**a**) zero applied static field in the 1.9 (red)–5.5 (blue) K temperature range, (**b**) 1.9 K and variable applied static field in the 0 (red)–50 (blue) kOe range, (**c**) 1 kOe applied static field in the 1.9 (red)–5.5 (blue) K temperature range; all measurements were performed in the 10–10,000 Hz frequency range, and grey lines are a guide for the eye. (**d**) Arrhenius plot for **Fe_4Ag** both at zero and 1-kOe applied static fields; black lines are given by fitting data with the Arrhenius law.

3. Materials and Methods

3.1. General Information

Reagent-grade 2-(4-bromophenyl)ethanol, pyridin-4-ylboronic acid, TICA, TEMPO radical, paraformaldehyde, $Pd(PPh_3)_4$, solvents and inorganic reagents for organic synthesis, $AgClO_4$, anhydrous toluene (VWR, max. 20 ppm H_2O) and anhydrous THF (VWR, max. 30 ppm H_2O) were used as received. Petroleum ether (PE) used was the 40–60 °C boiling fraction. EtOH was distilled over magnesium ethoxide and stored over 3 Å molecular sieves, while Et_2O was pre-dried over $CaCl_2$ overnight and distilled from sodium and benzophenone under N_2 before use. Elemental analyses were performed with a Carlo Erba EA1110 CHNS-O automatic analyzer. IR spectra were recorded as KBr discs by using a Jasco FTIR-4700 LE spectrophotometer with 2 cm^{-1} resolution; bands are reported as wavenumbers (cm^{-1}) together with the assignment and relative intensity (vs = very strong, s = strong, m = medium, w = weak, br = broad). Thin layer chromatography (TLC) was performed on silica gel and retention factors (r.f.) are reported for the given eluent. GC-MS analyses were performed with an HP GCD G1800C gas-chromatograph with injector and detector temperatures of 250 and 280 °C, respectively; the heating procedure started at 100 °C for 5 min, heated to 240 °C with a rate of 10 °C min^{-1}, and then kept at 240 °C for 16 min; retention times (r.t.) are given in minutes. ^{1}H and ^{13}C NMR spectra at 400 and 100 MHz, respectively, were recorded at room temperature with a Bruker Advance 400 spectrometer with chemical shifts given in parts per million (ppm) versus external TMS. The chemical shifts reported were determined by reference to the solvent residual signal (proton: 7.26, 2.50 and 2.08 ppm and carbon: 77.2, 39.5, and 20.4 ppm for $CDCl_3$, DMSO-d_6, and toluene-d_8, respectively); coupling constants are given in Hz. $[Fe_2(OEt)_2(dpm)_4]$ [33] and $[Fe_4(OMe)_6(dpm)_6]$ [12,32] were synthesized as previously reported in the literature. Synthesis of **3** and **4** and attempted synthesis of **H_3PhpPy** from **4** are reported in the Supplementary Materials.

3.2. Synthesis of 2-(4-(pyridin-4-yl)phenyl)ethanol (**1**)

This compound was obtained with a modification of a published procedure [28], especially in the final purification step. 2-(4-bromophenyl)ethanol (1.00 g, 4.97 mmol), pyridin-4-ylboronic acid (0.552 g, 4.49 mmol), and Na_2CO_3 (0.526 g, 4.97 mmol) were introduced in a Schlenk tube under Ar. Then, $Pd(PPh_3)_4$ (0.262 g, 0.23 mmol) was added together with the solvent mixture (DMF:H_2O 3:1, 24 mL overall). The yellow-green solution was kept under stirring at 110 °C for 24 h, and then it was cooled to room temperature and open to air to decompose any unreacted catalyst. The mixture was transferred in a round-bottom flask with the help of CH_2Cl_2 (2 × 5 mL). The volatile organic phase was removed under reduced pressure yielding a yellow-green residue still containing DMF, H_2O, or both. It was then transferred in a separating funnel and extracted with CH_2Cl_2 (40 mL) and H_2O (20 mL). The aqueous layer was further extracted with CH_2Cl_2 (2 × 10 mL), and the organic phases were washed with H_2O (10 mL). The aqueous phase was extracted with Et_2O (3 × 10 mL) and all the organic phases were unified and concentrated under reduced pressure, yielding a yellow-orange concentrated solution still containing some DMF. Both TLC (PE:AcOEt 1:4) and GC-MS analysis showed the presence of the desired product as main component of the mixture. This was then diluted with Et_2O (anhydrous over molecular sieves, 10 mL) and the resulting solution was treated with HCl (1.32 mol L^{-1} solution in Et_2O, 5.0 mL, 6.6 mmol), obtaining the efficient precipitation of the product as light yellow hydrochloride salt. After 5 min under stirring the solid was filtered on a Gooch G3 and washed with Et_2O (anhydrous over molecular sieves, 2 × 5 mL). The solid was then suspended in CH_2Cl_2 (20 mL) and aqueous NaOH (5% *w*/*w* solution, 4.5 mL, 5.62 mmol) was slowly added under stirring. The mixture was transferred in a separating funnel, the aqueous solution was extracted with further CH_2Cl_2 (5 mL) and the organic phases were unified, dried over $MgSO_4$ and taken to dryness under reduced pressure. The dense oil was dissolved in CH_2Cl_2 (4 mL) and Et_2O (15 mL) yielding a turbid yellow solution. This was refluxed for 5 min obtaining the precipitation of a brown solid, which was filtered off and discharged. The solution was then concentrated under reduced pressure till formation of a solid, then *n*-hexane (20 mL) was added and the mixture again concentrated under reduced pressure and cooled with an ice bath in order to favor the precipitation. The title compound as light yellow solid was filtered on a Gooch G3, washed with *n*-hexane (5 mL) and dried under vacuum (0.57 g, 58%). TLC (PE:AcOEt 1:4) r.f. = 0.14. GC-MS: r.t. = 18.55 min, m/z = 199 $[M]^+$. Elemental analysis calcd (%) for $C_{13}H_{13}NO$ (199.25): C 78.36, H 6.58, N 7.03; found: C 78.05, H 6.68, N 7.10. IR (KBr): $\tilde{\nu}$ = 3189 (br, ν O–H), 3043, 2997, 2943, 2919, and 2858 (m–s, ν C–H), 1603 (vs, ν C=N), 1495, 1424, 1406, and 1365 (s, ν aromatic C=C), 1236, 1207, and 1164 (s, ν aliphatic C–C), 1064 (vs, ν alkoxido C–O). ^{1}H NMR (400 MHz, 298 K, $CDCl_3$): δ 2.30 (br, 1H, OH), 2.95 (t, J = 6.49 Hz, 2H, H2), 3.93 (t, J = 6.49 Hz, 2H, H1), 7.37 (m, 2H, H4), 7.53 (m, 2H, H5), 7.60 (m, 2H, H8), 8.64 (m, 2H, H9) ppm. ^{13}C NMR (100 MHz, 298 K, $CDCl_3$): δ 38.9 (C2), 63.4 (C1), 121.7 (C8), 127.2 (C5), 129.9 (C4), 135.9 (C3), 140.3 (C6), 148.9 (C7), 149.4 (C9) ppm (see Scheme 1 for atom numbering).

3.3. Synthesis of 2-(4-(Pyridin-4-yl)phenyl)acetaldehyde (**2**)

This compound was obtained with a modification of a published procedure [29]. **1** (0.50 g, 2.51 mmol) was dissolved in CH_2Cl_2 (13 mL, anhydrous over molecular sieves) and the resulting solution was cooled with an ice bath. After 10 min, TICA (0.50 g, 2.15 mmol) was added yielding a white suspension, which was further stirred for 20 min at low temperature. TEMPO (0.073 mol L^{-1} solution in CH_2Cl_2, 0.30 mL, 0.022 mmol) was added, the reaction mixture left at 0 °C for 15 min, and then diluted with CH_2Cl_2 (7 mL). Aqueous Na_2CO_3 (1.5 mL of a saturated solution) was added observing a color change from orange to yellow and formation of a white solid. The liquid phase was separated, the solid residue was washed with CH_2Cl_2 (2 × 5 mL) and the organic phases taken to dryness under reduced pressure. The orange residue was dissolved in CH_2Cl_2 (8 mL) and Et_2O (10 mL), heated to reflux for 5 min, and the yellow liquid phase was filtered on a Gooch G3 to eliminate the solid and taken to dryness, yielding the title compound as yellow solid (0.47 g, 95%). TLC (PE:AcOEt 1:4) r.f. = 0.26. GC-MS: r.t. = 17.10 min, m/z = 197 $[M]^+$. Elemental analysis calcd (%) for $C_{13}H_{11}NO{\cdot}^1/_3H_2O$

(203.24): C 76.83, H 5.79, N 6.89; found: C 76.94, H 5.86, N 6.91. IR (KBr): $\tilde{v}$ = 1701 (s, ν C=O), 1596 (s, ν C=N), 1540, 1488 and 1403 (m, ν aromatic C=C). ^{1}H NMR (400 MHz, 298 K, $CDCl_3$): δ 3.81 (d, J = 1.99 Hz, 2H, H2), 7.38 (m, 2H, H4), 7.66 (m, 2H, H8), 7.71 (m, 2H, H5), 8.70 (m, 2H, H9), 9.82 (t, J = 1.99 Hz, 1H, H1) ppm. ^{13}C NMR (100 MHz, 298 K, $CDCl_3$): δ 50.2 (C2), 122.3 (C8), 127.8 (C5), 130.7 (C4), 134.1 (C3), 136.1 (C6), 147.4 (C7), 150.5 (C9), 198.4 (C1) ppm (see Scheme 1 for atom numbering).

*3.4. Synthesis of 2-(Hydroxymethyl)-2-(4-(pyridin-4-yl)phenyl)propane-1,3-diol (***H_3PhpPy***)*

2 (0.50 g, 2.54 mmol), paraformaldehyde (0.50 g, 16.7 mmol), $Ca(OH)_2$ (0.25 g, 3.37 mmol) and $Al(O$*i*$Pr)_3$ (0.05 g, 0.24 mmol) were dissolved in THF (5.5 mL, anhydrous over molecular sieves) in a Schlenk tube under Ar atmosphere. The mixture was stirred at 60 °C for 3 days, then cooled to room temperature, diluted with fresh THF (20 mL) and filtered on a Gooch G3 and Celite, washing with THF (2 × 10 mL). The obtained yellow solution was taken to dryness under reduced pressure, and the crude orange dense oil was purified with column chromatography (h = 17.0 cm, Ø = 2.5 cm) over silica gel and PE:AcOEt:THF (10:85:5, 100 mL), AcOEt:THF (95:5, 100 mL), AcOEt:THF:EtOH (95:2.5:2.5, 100 mL), AcOEt:EtOH (95:5, 200 mL) and AcOEt:EtOH (90:10, 200 mL) as eluent. The title compound was obtained as light yellow solid by removing of the solvent under reduced pressure of the fractions containing the desired product, washing it with $CHCl_3$ (1.5 mL) and drying under vacuum (0.27 g, 41%). TLC (AcOEt:EtOH 9:1) r.f. = 0.11. GC-MS: not performed due to the high affinity of the triol unit for the stationary phase of the column. Elemental analysis calcd (%) for $C_{15}H_{17}NO_3 \cdot 0.6H_2O$ (270.11): C 66.70, H 6.79, N 5.19; found: C 66.66, H 6.67, N 4.91. IR (KBr): $\tilde{v}$ = 3354 and 3255 (br, ν O–H), 2946 and 2887 (m, ν C–H), 1602 (vs, ν C=N), 1491 and 1406 (m–s, ν C=C), 1025 (vs, ν alkoxido C–O). ^{1}H NMR (400 MHz, 298 K, DMSO-d_6): δ 3.77 (s, 6H, H1), 4.48 (br, 3H, OH), 7.58 (m, 2H, H5), 7.69 (m, 2H, H8), 7.71 (m, 2H, H4), 8.62 (m, 2H, H9). ^{13}C NMR (100 MHz, 298 K, DMSO-d_6): δ 49.3 (C2), 63.3 (C1), 121.2 (C8), 125.9 (C4), 128.6 (C5), 134.2 (C6), 144.7 (C7), 147.3 (C3), 150.0 (C9) (see Scheme 1 for atom numbering).

3.5. Synthesis of [$Fe_4(PhpPy)_2(dpm)_6$*] (***Fe_4***)*

A suspension of **H_3PhpPy** (21.5 mg, 0.0829 mmol) in distilled EtOH (3.5 mL) was added dropwise to an orange solution of $[Fe_4(OMe)_6(dpm)_6]$ (50.0 mg, 0.0331 mmol) in distilled Et_2O (21.0 mL). The reaction mixture became turbid and darker orange, and after 5 h under stirring at room temperature it was filtered to eliminate the undissolved material. The clear orange solution was taken to dryness yielding an orange powder, which appeared homogeneous under visual inspection at the microscope. IR (KBr): $\tilde{v}$ = 2962 (s, ν C–H), 1564, 1546, 1536, and 1505 (vs, ν C=N, C=O), 1401, 1385 and 1357 (s, ν aliphatic C–C), 1096 (m, ν alkoxido C–O), 566 (w, ν Fe–O). ^{1}H NMR (400 MHz, 298 K, toluene-d_8): δ 6.5, 8.8, 10.9, 12.0, 13.1 ppm. MS ESI (CH_3CN): 644.4 ($[Fe(dpm)_3 + K]^+$, 50%), 1835.8 ($[$**Fe_4** $+ H]^+$, 10), 1874.7 ($[$**Fe_4** $+ K]^+$, 100). Elemental analysis calcd (%) for $C_{96}H_{142}Fe_4N_2O_{18}$ (1835.54): C 62.82, H 7.80, N 1.53; found for powder: C 62.94, H 8.07, N 1.81. Different attempts to crystallize the title cluster by vapor diffusion of EtOH or evaporation of the mother liquor always yielded the dimer $[Fe_2(OEt)_2(dpm)_4]$ as main component; in one case we could also isolate single crystals of **Fe_4** suitable for X-ray diffraction. Elemental analysis calcd (%) for $C_{96}H_{142}Fe_4N_2O_{18}$ (1835.54): C 62.82, H 7.80, N 1.53; found for manually-selected crystals: C 62.98, H 7.86, N 1.56.

3.6. Synthesis of {[$Fe_4(PhpPy)_2(dpm)_6Ag](ClO_4)$*}$_n$ (***Fe_4Ag***)*

A solution of **Fe_4** (obtained from 25.0 mg of $[Fe_4(OMe)_6(dpm)_6]$, 0.0165 mol) in anhydrous toluene (4.0 mL), was put in liquid/liquid diffusion with a solution of $AgClO_4$ in anhydrous THF (1.8 mL of a 9.12×10^{-3} mol L^{-1} solution, 0.0164 mmol). After one week the diffusion was complete and the orange needle-like microcrystals formed at the interface were filtered, washed with a toluene:THF 2:1 mixture and dried under vacuum (23.9 mg, 71.3%). Elemental analysis calcd (%) for $C_{96}H_{142}AgClFe_4N_2O_{22}$ (2042.86): C 56.44, H 7.01, N 1.37; found: C 56.81, H 6.92, N 1.41. IR (KBr): $\tilde{v}$ = 3434 (br), 2963 (s, ν C–H), 1564, 1548, and 1505 (vs, ν C=N and C=O), 1400, 1385, and 1357 (s, ν aliphatic C–C), 1122 (m, ν

ClO_4), 1092 (m, ν alkoxido C–O), 567 (w, ν Fe–O), 479 (w, ν Ag–N). MS ESI (THF/CH_3CN): m/z 1230.9 ([Fe_3(PhpPy)(dpm)$_4$(CH_3CN) + H + Na]$^+$, 100%), 1836.4 ([**Fe$_4$** + H]$^+$, 10), 1837.8 ([**Fe$_4$** + K]$^+$, 55), 2014.7 ([**Fe$_4$**Ag(THF)]$^+$, 5).

3.7. X-ray Data Collection and Structure Determination

Crystals of **Fe$_4$** suitable for X-ray diffraction experiments were selected from the mother liquor in EtOH/Et_2O. Intensity data were collected on a Bruker Apex CCD area detector using graphite monochromatic Mo-$K\alpha$ radiation. Crystal structure data for **Fe$_4$**: $C_{96}H_{142}Fe_4N_2O_{18}$, M_r = 1835.54, crystal dimensions 0.37 × 0.15 × 0.15 mm, monoclinic, space group: $C2/c$ (No. 15), a = 19.328(3), b = 23.163(3), c = 24.483(4) Å, β = 108.155(2), V = 10,416(3) Å^3, Z = 4, ρ_{calc} = 1.171 g cm^{-3}, $2\theta_{max}$ = 46.78°, T = 293(2) K, collected/independent reflections = 55,040/7575, R(int) = 0.0644, parameters/restraints = 651/108, final R indices: R_1 = 0.0561, wR_2 = 0.1384 [on 5266 reflections with $I > 2\sigma(I)$], R_1 = 0.0859, wR_2 = 0.1690 [all data], goodness-of-fit = 1.074.

During data collection, no crystal decay was observed, so that no time-decay correction was needed. Data reductions were performed with SAINT, and absorption corrections based on multiscan were obtained with SADABS [48]. The structure was solved by direct methods and refined with SHELXL-2016/6 [49] implemented in WinGX—Version 2014.1 system [50]. The program ORTEPIII was used for graphics [51]. Three over six *t*Bu groups were refined for their disorder by splitting them into two positions, A and B, with complementary occupancy factors of 0.624(15) and 0.376(15); restraint ISOR (sigma = 0.1) was also applied to the disordered terminal carbon atoms to ensure reasonable thermal ellipsoids. Anisotropic thermal parameters were used for all non-H atoms. The isotropic thermal parameters of H atoms were fixed at 1.2 (1.5 for methyl groups) times those of the atom to which they were attached. All H atoms were placed in calculated positions and refined by a riding model.

CCDC 1842624 contains the supplementary crystallographic data for **Fe$_4$**. These data can be obtained free of charge via http://www.ccdc.cam.ac.uk/conts/retrieving.html, or from the Cambridge Crystallographic Data Centre, 12 Union Road, Cambridge CB2 1EZ, UK; fax: (+44) 1223-336-033, or e-mail: deposit@ccdc.cam.ac.uk.

3.8. Magnetic Measurements

Dc magnetic data were recorded using a Quantum Design MPMS SQUID magnetometer. Magnetic susceptibilities were measured on 7.54 and 8.10 mg powder samples of **Fe$_4$** and **Fe$_4$Ag**, respectively, packed in a Teflon pellet with applied fields of 1 kOe from 1.9 (**Fe$_4$Ag**) or 5 (**Fe$_4$**) to 40 K and of 10 kOe from 40 to 300 (**Fe$_4$Ag**) or 250 (**Fe$_4$**) K. Data reduction was carried out by using 1835.54 and 2042.86 as molecular weights and −1054.9 and −1114.9 10^{-6} emu mol^{-1} as diamagnetic contributions, estimated from the Pascal's constants [52], for **Fe$_4$** and **Fe$_4$Ag**, respectively. Data fitting was performed by using program PHI v3.1.1 [44]. Ac susceptibility was recorded on a Quantum Design PPMS susceptometer for **Fe$_4$Ag** at zero static applied field and for both **Fe$_4$** and **Fe$_4$Ag** samples at 1 kOe static applied field, while the previously reported Quantum Design MPMS SQUID was employed for ac measurements on **Fe$_4$** at zero static applied field.

4. Conclusions

As a promising strategy in developing the performance of SMMs by their assembly into coordination networks, in this paper we have described the behavior of a tetrairon(III) cluster, **Fe$_4$**, as longer spacer (23.4 Å) when coordinating to silver(I) ions, in comparison with what previously observed with a shorter spacer (14.8 Å) of the same family, **A** [14]. As crucial point when engineering novel compounds with desired properties [53], the chemical design of the suitable tripodal ligand and its synthesis revealed fundamental for this project. 1D polymer chains were achieved in **Fe$_4$Ag** with **Fe$_4$**:$AgClO_4$ 1:1 ratio, in contrast with the aimed 3D arrangement similar to **B**, which contains an **A**:$AgClO_4$ 2:1 ratio [14]. The enormous cavities that would have formed with a 3D-MOF structure

given by an **Fe$_4$**:$AgClO_4$ 2:1 ratio might probably suffer of high instability in the absence of any supplementary big molecules acting as sustain within the pores, and this point will be pursued in our future studies.

Despite the synthesized coordination polymer **Fe$_4$Ag** does not possess the desired 3D structure, it still revealed invariant relaxation dynamics compared to **B**, in which Fe_4 SMMs behave as building blocks of polymeric structures. Further work to address 1D vs. 3D issue will be perceived also by testing other metal ions or coordination units like ruthenium dimers, which hold minor flexibility in their coordination behavior with respect to silver(I). In fact, this ion can assume different coordination environments only by subtle changes in the surrounding environment or the donor power of the coordinated atoms [43,54,55], as we could clearly observe here by exchanging H_3pPy with **H$_3$PhpPy** and that highlights how small molecular modifications can direct the fate of the final supramolecular assembly.

Supplementary Materials: The following are available online at http://www.mdpi.com/2312-7481/4/4/43/s1, Experimental Section (cont.): Synthesis of **3** and **4**, Scheme S1: synthetic path of **H$_3$PhpPy** through **3** and **4**; Figure S1: Crystal packing in **Fe$_4$** with highlighted weak $\pi\cdots\pi$ stacking interactions; Figure S2: ESI-MS spectrum in THF/CH_3CN of the reaction mixture for the synthesis of **Fe$_4$** after 5 h of stirring in EtOH at room temperature; Figure S3: Comparison among the infrared spectra of $[Fe_2(OEt)_2(dpm)_4]$, $[Fe_4(OMe)_6(dpm)_6]$ and **Fe$_4$** as KBr disks; Figure S4: ^{1}H NMR spectrum of **Fe$_4$** in toluene-d_8 at room temperature; Figure S5: ESI-MS spectrum in THF/CH_3CN of **Fe$_4$Ag**; Figure S6: Comparison among the infrared spectra of **Fe$_4$** and **Fe$_4$Ag** as KBr disks; Figure S7: XRF spectrum of **Fe$_4$Ag** with a view of the orange microcrystals; Figure S8: Temperature dependence of $\chi_M T$ for **Fe$_4$**; Figure S9: Imaginary component of the ac susceptibility, χ''_M, of **Fe$_4$** measured at zero and 1-kOe applied static fields together with the corresponding $\ln(\tau)$-vs.-$1/T$ Arrhenius plots.

Author Contributions: Conceptualization, L.R.; Data curation, L.R., C.B., and A.F.; Formal analysis, M.V. and C.B.; Investigation, L.R., M.V., F.R., and A.F.; Methodology, M.V. and F.R.; Project administration, L.R.; Resources, L.R., F.R., and A.F.; Supervision, L.R.; Writing–review & editing, L.R.

Funding: This project was founded by the European Research Council and the Italian Ministero dell'Istruzione, dell'Università e della Ricerca (MIUR) through the Advanced Grant MolNanoMaS no. 267746 and the FIRB project no. RBAP117RWN, respectively.

Acknowledgments: Authors would like to thank Carri Cotton (Erasmus student at Università degli Studi di Modena e Reggio Emilia from Warwick University, UK) for some preliminary synthetic work, Giorgia Ferrari for helping in XRF analysis, Andrea Nava for helping in preliminary single-crystal analyses, Andrea Cornia (Dipartimento di Scienze Chimiche e Geologiche, Università degli Studi di Modena e Reggio Emilia) for the access to the facilities of his research laboratory, and Roberta Sessoli and the Laboratory of Molecular Magnetism (Dipartimento di Chimica 'Ugo Schiff', Università degli Studi di Firenze) for the access to the facilities for magnetic measurements. L.R. also thanks Valentina Nicolini (Università degli Studi di Modena e Reggio Emilia) for helpful hints while writing the paper.

Conflicts of Interest: The authors declare no conflict of interest. The founding sponsors had no role in the design of the study; in the collection, analyses, or interpretation of data; in the writing of the manuscript, and in the decision to publish the results.

References

1. Gatteschi, D.; Sessoli, R.; Villain, J. *Molecular Nanomagnets*; Oxford University Press: Oxford, UK, 2006; ISBN 978-0-19-856753-0.
2. Natterer, F.D.; Yang, K.; Paul, W.; Willke, P.; Choi, T.; Greber, T.; Heinrich, A.J.; Lutz, C.P. Reading and writing single-atom magnets. *Nature* **2017**, *543*, 226–228. [CrossRef] [PubMed]
3. Goodwin, C.A.P.; Ortu, F.; Reta, D.; Chilton, N.F.; Mills, D.P. Molecular magnetic hysteresis at 60 kelvin in dysprosocenium. *Nature* **2017**, *548*, 439–442. [CrossRef] [PubMed]
4. Guo, F.-S.; Day, B.M.; Chen, Y.-C.; Tong, M.-L.; Mansikkamäki, A.; Layfield, R.A. A Dysprosium Metallocene Single-Molecule Magnet Functioning at the Axial Limit. *Angew. Chem. Int. Ed.* **2017**, *56*, 11445–11449. [CrossRef] [PubMed]
5. Liu, K.; Zhang, X.; Meng, X.; Shi, W.; Cheng, P.; Powell, A.K. Constraining the coordination geometries of lanthanide centers and magnetic building blocks in frameworks: A new strategy for molecular nanomagnets. *Chem. Soc. Rev.* **2016**, *45*, 2423–2439. [CrossRef] [PubMed]

6. Whitehead, G.F.S.; Moro, F.; Timco, G.A.; Wernsdorfer, W.; Teat, S.J.; Winpenny, R.E.P. A Ring of Rings and Other Multicomponent Assemblies of Cages. *Angew. Chem. Int. Ed.* **2013**, *52*, 9932–9935. [CrossRef] [PubMed]
7. Jeon, I.-R.; Clérac, R. Controlled association of single-molecule magnets (SMMs) into coordination networks: Towards a new generation of magnetic materials. *Dalton Trans.* **2012**, *41*, 9569–9586. [CrossRef] [PubMed]
8. Kostakis, G.E.; Hewitt, I.J.; Ako, A.M.; Mereacre, V.; Powell, A.K. Magnetic coordination clusters and networks: Synthesis and topological description. *Philos. Trans. R. Soc. Math. Phys. Eng. Sci.* **2010**, *368*, 1509–1536. [CrossRef] [PubMed]
9. Roubeau, O.; Clérac, R. Rational Assembly of High-Spin Polynuclear Magnetic Complexes into Coordination Networks: The Case of a [Mn_4] Single-Molecule Magnet Building Block. *Eur. J. Inorg. Chem.* **2008**, *2008*, 4325–4342. [CrossRef]
10. Abstracts from the X INSTM National Conference on Materials Science and Technology. *J. Appl. Biomater. Funct. Mater.* **2016**, *14*, e84–e128. [CrossRef]
11. Nava, A.; Rigamonti, L.; Zangrando, E.; Sessoli, R.; Wernsdorfer, W.; Cornia, A. Redox-Controlled Exchange Bias in a Supramolecular Chain of Fe_4 Single-Molecule Magnets. *Angew. Chem. Int. Ed.* **2015**, *54*, 8777–8782. [CrossRef] [PubMed]
12. Accorsi, S.; Barra, A.-L.; Caneschi, A.; Chastanet, G.; Cornia, A.; Fabretti, A.C.; Gatteschi, D.; Mortalò, C.; Olivieri, E.; Parenti, F.; et al. Tuning Anisotropy Barriers in a Family of Tetrairon(III) Single-Molecule Magnets with an $S = 5$ Ground State. *J. Am. Chem. Soc.* **2006**, *128*, 4742–4755. [CrossRef] [PubMed]
13. Gregoli, L.; Danieli, C.; Barra, A.-L.; Neugebauer, P.; Pellegrino, G.; Poneti, G.; Sessoli, R.; Cornia, A. Magnetostructural Correlations in Tetrairon(III) Single-Molecule Magnets. *Chem. Eur. J.* **2009**, *15*, 6456–6467. [CrossRef] [PubMed]
14. Rigamonti, L.; Cotton, C.; Nava, A.; Lang, H.; Rüffer, T.; Perfetti, M.; Sorace, L.; Barra, A.-L.; Lan, Y.; Wernsdorfer, W.; et al. Diamondoid Structure in a Metal-Organic Framework of Fe_4 Single-Molecule Magnets. *Chem. Eur. J.* **2016**, *22*, 13705–13714. [CrossRef] [PubMed]
15. Rigamonti, L.; Piccioli, M.; Malavolti, L.; Poggini, L.; Mannini, M.; Totti, F.; Cortigiani, B.; Magnani, A.; Sessoli, R.; Cornia, A. Enhanced Vapor-Phase Processing in Fluorinated Fe_4 Single-Molecule Magnets. *Inorg. Chem.* **2013**, *52*, 5897–5905. [CrossRef] [PubMed]
16. Rigamonti, L.; Piccioli, M.; Nava, A.; Malavolti, L.; Cortigiani, B.; Sessoli, R.; Cornia, A. Structure, magnetic properties and thermal sublimation of fluorinated Fe_4 Single-Molecule Magnets. *Polyhedron* **2017**, *128*, 9–17. [CrossRef]
17. Ninova, S.; Lanzilotto, V.; Malavolti, L.; Rigamonti, L.; Cortigiani, B.; Mannini, M.; Totti, F.; Sessoli, R. Valence electronic structure of sublimated Fe_4 single-molecule magnets: An experimental and theoretical characterization. *J. Mater. Chem. C* **2014**, *2*, 9599–9608. [CrossRef]
18. Mannini, M.; Pineider, F.; Danieli, C.; Totti, F.; Sorace, L.; Sainctavit, P.; Arrio, M.-A.; Otero, E.; Joly, L.; Cezar, J.C.; et al. Quantum tunnelling of the magnetization in a monolayer of oriented single-molecule magnets. *Nature* **2010**, *468*, 417–421. [CrossRef] [PubMed]
19. Rodriguez-Douton, M.J.; Mannini, M.; Armelao, L.; Barra, A.-L.; Tancini, E.; Sessoli, R.; Cornia, A. One-step covalent grafting of Fe_4 single-molecule magnet monolayers on gold. *Chem. Commun.* **2011**, *47*, 1467–1469. [CrossRef] [PubMed]
20. Mannini, M.; Tancini, E.; Sorace, L.; Sainctavit, P.; Arrio, M.-A.; Qian, Y.; Otero, E.; Chiappe, D.; Margheriti, L.; Cezar, J.C.; et al. Spin Structure of Surface-Supported Single-Molecule Magnets from Isomorphous Replacement and X-ray Magnetic Circular Dichroism. *Inorg. Chem.* **2011**, *50*, 2911–2917. [CrossRef] [PubMed]
21. Tancini, E.; Mannini, M.; Sainctavit, P.; Otero, E.; Sessoli, R.; Cornia, A. On-Surface Magnetometry: The Evaluation of Superexchange Coupling Constants in Surface-Wired Single-Molecule Magnets. *Chem. Eur. J.* **2013**, *19*, 16902–16905. [CrossRef] [PubMed]
22. Westrup, K.C.M.; Boulon, M.-E.; Totaro, P.; Nunes, G.G.; Back, D.F.; Barison, A.; Jackson, M.; Paulsen, C.; Gatteschi, D.; Sorace, L.; et al. Adding Remnant Magnetization and Anisotropic Exchange to Propeller-like Single-Molecule Magnets through Chemical Design. *Chem. Eur. J.* **2014**, *20*, 13681–13691. [CrossRef] [PubMed]

23. Rigamonti, L.; Cornia, A.; Nava, A.; Perfetti, M.; Boulon, M.-E.; Barra, A.-L.; Zhong, X.; Park, K.; Sessoli, R. Mapping of single-site magnetic anisotropy tensors in weakly coupled spin clusters by torque magnetometry. *Phys. Chem. Chem. Phys.* **2014**, *16*, 17220–17230. [CrossRef] [PubMed]
24. Rigamonti, L.; Nava, A.; Boulon, M.-E.; Luzon, J.; Sessoli, R.; Cornia, A. Experimental and Theoretical Studies on the Magnetic Anisotropy in Lanthanide(III)-Centered Fe_3Ln Propellers. *Chem. Eur. J.* **2015**, *21*, 12171–12180. [CrossRef] [PubMed]
25. Burgess, J.A.J.; Malavolti, L.; Lanzilotto, V.; Mannini, M.; Yan, S.; Ninova, S.; Totti, F.; Rolf-Pissarczyk, S.; Cornia, A.; Sessoli, R.; et al. Magnetic fingerprint of individual Fe_4 molecular magnets under compression by a scanning tunnelling microscope. *Nat. Commun.* **2015**, *6*, 8216. [CrossRef] [PubMed]
26. Zu, F.; Liu, Z.; Yao, K.; Gao, G.; Fu, H.; Zhu, S.; Ni, Y.; Peng, L. Nearly Perfect Spin Filter, Spin Valve and Negative Differential Resistance Effects in a Fe_4-based Single-molecule Junction. *Sci. Rep.* **2015**, *4*, 4838. [CrossRef] [PubMed]
27. Batten, S.R.; Champness, N.R.; Chen, X.-M.; Garcia-Martinez, J.; Kitagawa, S.; Öhrström, L.; O'Keeffe, M.; Paik Suh, M.; Reedijk, J. Terminology of metal–organic frameworks and coordination polymers (IUPAC Recommendations 2013). *Pure Appl. Chem.* **2013**, *85*, 1715–1724. [CrossRef]
28. Vukotic, V.N.; Loeb, S.J. One-, Two- and Three-Periodic Metal-Organic Rotaxane Frameworks (MORFs): Linking Cationic Transition-Metal Nodes with an Anionic Rotaxane Ligand. *Chem. Eur. J.* **2010**, *16*, 13630–13637. [CrossRef] [PubMed]
29. Condorelli, G.G.; Motta, A.; Pellegrino, G.; Cornia, A.; Gorini, L.; Fragalà, I.L.; Sangregorio, C.; Sorace, L. Site-Specific Anchoring of Tetrairon(III) Single Molecule Magnets on Functionalized Si(100) Surfaces. *Chem. Mater.* **2008**, *20*, 2405–2411. [CrossRef]
30. Viguier, R.; Serratrice, G.; Dupraz, A.; Dupuy, C. New Polypodal Polycarboxylic Ligands—Complexation of Rare-Earth Ions in Aqueous Solution. *Eur. J. Inorg. Chem.* **2001**, 1789–1795. [CrossRef]
31. Beaufort, L.; Delaude, L.; Noels, A.F. A new tripodal ligand system based on the iminophosphorane functional group. Part 1: Synthesis and characterization. *Tetrahedron* **2007**, *63*, 7003–7008. [CrossRef]
32. Barra, A.L.; Caneschi, A.; Cornia, A.; Fabrizi de Biani, F.; Gatteschi, D.; Sangregorio, C.; Sessoli, R.; Sorace, L. Single-Molecule Magnet Behavior of a Tetranuclear Iron(III) Complex. The Origin of Slow Magnetic Relaxation in Iron(III) Clusters. *J. Am. Chem. Soc.* **1999**, *121*, 5302–5310. [CrossRef]
33. Wu, C.-H.S.; Rossman, G.R.; Gray, H.B.; Hammond, G.S.; Schugar, H.J. Chelates of β-diketones. VI. Synthesis and characterization of dimeric dialkoxo-bridged iron(III) complexes with acetylacetone and 2,2,6,6-tetramethylheptane-3,5-dione (HDPM). *Inorg. Chem.* **1972**, *11*, 990–994. [CrossRef]
34. Rigamonti, L.; Rusconi, M.; Forni, A.; Pasini, A. The role of the atomic charges on the ligands and platinum(II) in affecting the cis and trans influences in $[PtXL(PPh_3)_2]^+$ complexes (X = NO_3, Cl, Br, I.; L = 4-substituted pyridines, amines, PPh_3). A ^{31}P NMR and DFT investigation. *Dalton Trans.* **2011**, *40*, 10162. [CrossRef] [PubMed]
35. Nakamoto, K. *Infrared and Raman Spectra of Inorganic and Coordination Compounds*, 6th ed.; Wiley: Hoboken, NJ, USA, 2009; ISBN 978-0-471-74339-2.
36. Geddes, A.L.; Bottger, G.L. Infrared spectra of silver-ammine complexes. *Inorg. Chem.* **1969**, *8*, 802–807. [CrossRef]
37. Kondo, J.; Tada, Y.; Dairaku, T.; Saneyoshi, H.; Okamoto, I.; Tanaka, Y.; Ono, A. High-Resolution Crystal Structure of a Silver(I)-RNA Hybrid Duplex Containing Watson-Crick-like C-Silver(I)-C Metallo-Base Pairs. *Angew. Chem. Int. Ed.* **2015**, *54*, 13323–13326. [CrossRef] [PubMed]
38. Kim, J.G.; Cho, Y.; Lee, H.; Lee, Y.-A.; Jung, O.-S. *o*-, *m*-, and *p*-Pyridyl isomer effects on construction of 1D loop-and-chains: Silver(I) coordination polymers with Y-type tridentate ligands. *J. Mol. Struct.* **2016**, *1122*, 186–191. [CrossRef]
39. Zhu, H.-L.; Zhang, M.; Sun, Z.-Y.; Rong, N.-N.; Zhang, B.; Li, Y.; Fun, H.-K. Crystal structure of di(4-aminopyridine)silver(I) trifluoromethylsulfate, $Ag(C_5H_6N_2)_2(CF_3SO_3)$. *Z. Für Krist. New Cryst. Struct.* **2003**, *218*, 521–522. [CrossRef]
40. Liu, J.-T.; Ng, S.W. *catena*-Poly[[silver-μ-piperazine-κ^2N:N']perchlorate]. *Acta Crystallogr. Sect. E Struct. Rep. Online* **2006**, *62*, m1992–m1993. [CrossRef]
41. Cong, F.-D.; Yu, F.-Y.; Wei, Z.; Ng, S.W. Bis(2-methyl-1*H*-imidazole-κN^3)silver(I) nitrate dihydrate. *Acta Crystallogr. Sect. E Struct. Rep. Online* **2009**, *65*, m1535. [CrossRef] [PubMed]

42. Massoud, A.A.; Gohar, Y.M.; Langer, V.; Lincoln, P.; Svensson, F.R.; Jänis, J.; Gårdebjer, S.T.; Haukka, M.; Jonsson, F.; Aneheim, E.; et al. Bis 4,5-diazafluoren-9-one silver(I) nitrate: Synthesis, X-ray structures, solution chemistry, hydrogel loading, DNA coupling and anti-bacterial screening. *New J. Chem.* **2011**, *35*, 640–648. [CrossRef]
43. Shimokawa, C.; Itoh, S. The First β-Diketiminate−Ag(I) Complexes. Macrocyclic Dinuclear and Tetranuclear Ag(I)-Complexes and Linear Coordination Polymer Ag(I)-Complex. *Inorg. Chem.* **2005**, *44*, 3010–3012. [CrossRef] [PubMed]
44. Chilton, N.F.; Anderson, R.P.; Turner, L.D.; Soncini, A.; Murray, K.S. PHI: A powerful new program for the analysis of anisotropic monomeric and exchange-coupled polynuclear *d*- and *f*-block complexes. *J. Comput. Chem.* **2013**, *34*, 1164–1175. [CrossRef] [PubMed]
45. Cole, K.S.; Cole, R.H. Dispersion and Absorption in Dielectrics I. Alternating Current Characteristics. *J. Chem. Phys.* **1941**, *9*, 341–351. [CrossRef]
46. Dekker, C.; Arts, A.F.M.; de Wijn, H.W.; van Duyneveldt, A.J.; Mydosh, J.A. Activated dynamics in a two-dimensional Ising spin glass: $Rb_2Cu_{1-x}Co_xF_4$. *Phys. Rev. B* **1989**, *40*, 11243–11251. [CrossRef]
47. Lunghi, A.; Totti, F.; Sessoli, R.; Sanvito, S. The role of anharmonic phonons in under-barrier spin relaxation of single molecule magnets. *Nat. Commun.* **2017**, *8*, 14620. [CrossRef] [PubMed]
48. Bruker. *SMART, SAINT and SADABS*; Bruker AXS Inc.: Madison, WI, USA, 1997.
49. Sheldrick, G.M. Crystal structure refinement with SHELXL. *Acta Crystallogr. Sect. C Struct. Chem.* **2015**, *71*, 3–8. [CrossRef] [PubMed]
50. Farrugia, L.J. WinGX and ORTEP for Windows: An update. *J. Appl. Crystallogr.* **2012**, *45*, 849–854. [CrossRef]
51. Burnett, M.N.; Johnson, C.K. *ORTEP-III: Oak Ridge Thermal Ellipsoid Plot Program for Crystal Structure Illustrations*; U.S. Department of Energy Office of Scientific and Technical Information: Oak Ridge, TN, USA, 1996.
52. Bain, G.A.; Berry, J.F. Diamagnetic Corrections and Pascal's Constants. *J. Chem. Educ.* **2008**, *85*, 532–536. [CrossRef]
53. Rigamonti, L.; Bridonneau, N.; Poneti, G.; Tesi, L.; Sorace, L.; Pinkowicz, D.; Jover, J.; Ruiz, E.; Sessoli, R.; Cornia, A. A Pseudo-Octahedral Cobalt(II) Complex with bis-Pyrazolylpyridine Ligands Acting as a Zero-Field Single-Molecule Magnet with Easy Axis Anisotropy. *Chem. Eur. J.* **2018**, *24*, 8857–8868. [CrossRef] [PubMed]
54. Fox, B.S.; Beyer, M.K.; Bondybey, V.E. Coordination Chemistry of Silver Cations. *J. Am. Chem. Soc.* **2002**, *124*, 13613–13623. [CrossRef] [PubMed]
55. Shoeib, T.; El Aribi, H.; Siu, K.W.M.; Hopkinson, A.C. A Study of Silver(I) Ion−Organonitrile Complexes: Ion Structures, Binding Energies, and Substituent Effects. *J. Phys. Chem. A* **2001**, *105*, 710–719. [CrossRef]